WRF-ELM v1.0: a Regional Climate Model to Study Land-Atmosphere Interactions Over Heterogeneous Land Use Regions

Huilin Huang[1*], Yun Qian[1*], Gautam Bisht[1], Jiali Wang[2], Tirthankar Chakraborty[1], Dalei Hao[1], Jianfeng Li[1], Travis Thurber[1], Balwainder Singh[1], Zhao Yang[1], Ye Liu[1], Pengfei Xue[2,3], William J. Sacks[4], Ethan Coon[5], and Robert Hetland[1]

1. Atmospheric, Climate, and Earth Sciences Division, Pacific Northwest National Laboratory, Richland, WA, USA

2. Environmental Science Division, Argonne National Laboratory, Lemont, IL, USA.

3. Great Lakes Research Center, Michigan Technology University, Houghton, MI, USA.

4. Climate & Global Dynamics Lab, NSF National Center for Atmospheric Research, CO, USA

5. Climate Change Science Institute, Oak Ridge National Laboratory, TN, USA

Corresponding to: Huilin Huang (huilin.huang@pnnl.gov) and Yun Qian (yun.qian@pnnl.gov)

Target Journal

Geoscientific Model Development

Abstract

The Energy Exascale Earth System Model (E3SM) Land Model (ELM) is a state-of-the-art land surface model that simulates the intricate interactions between the terrestrial land surface and other components of the Earth system. Originating from the Community Land Model (CLM) version 4.5, ELM has been under active development, with added new features and functionality, including plant hydraulics, radiation-topography interaction, subsurface multiphase flow, and more explicit land use and management practices. This study integrates ELM v2.1 with the Weather Research and Forecasting (WRF) Model through a modified Lightweight Infrastructure for Land Atmosphere Coupling (LILAC) framework, enabling affordable high-resolution regional modeling by leveraging ELM's innovative features alongside WRF's diverse atmospheric parameterization options. This framework includes a top-level driver for variable communication between WRF and ELM and Earth System Modeling Framework (ESMF) caps for WRF atmospheric component and ELM workflow control, encompassing initialization, execution, and finalization. Importantly, this LILAC-ESMF framework demonstrates a more modular approach compared to previous coupling efforts between WRF and land surface models. It maintains the integrity of the ELM's source code structure and facilitates the transfer of future developments in ELM to WRF-ELM.

To test the ability of the coupled model in capturing land-atmosphere interactions over regions with a variety of land uses and land covers, we conducted high-resolution (4 km) WRF-ELM ensemble simulations over the Great Lakes Region (GLR) in the summer of 2018 and systematically compared the results against observations, reanalysis data, and WRF-CTSM (WRF-coupled with the Community Terrestrial Systems Model). In general, the coupled WRF-ELM model has reasonably captured the spatial distribution of surface state variables and fluxes across the GLR, particularly over the natural vegetation areas. The evaluation results provide a baseline reference for further improvements of ELM in the regional application of high-resolution weather and climate predictions. Our work serves as an example to the model development community for expanding an advanced land surface model's capability to represent fully-coupled land-atmosphere interactions at fine spatial scales. The development and release of WRF-ELM marks a significant advancement for the ELM user community, providing opportunities for fine-scale

48 regional representation, parameter calibration in coupled mode, and examination of new schemes with

49 atmospheric feedback.

1. Introduction

Land surface models (LSMs) solve the exchange of water, energy, and carbon fluxes between the land surface and atmosphere (Fisher and Koven, 2020), and are frequently used to simulate response of the Earth's surface to both anthropogenic and natural forcings (Best et al., 2015). These models describe biogeophysical properties like surface roughness, albedo, and evapotranspiration efficiency, characteristics crucial for modeling the land's influence on meteorological processes (Xue et al., 1991; Dai et al., 2003; Dickinson, 1984; Sellers et al., 1986). Originally developed to support weather and climate modeling, LSMs were designed to provide essential lower boundary conditions such as radiation, energy, and water fluxes to the atmosphere.

Over time, LSMs have evolved significantly, with representations of increasingly complex processes that impact land surface dynamics and belowground processes, with their feedback to the atmosphere being incrementally added in newer-generation LSMs. As a consequence of all these advancements, the applicability and scope of LSMs has broadened substantially from their initial versions, introducing sophisticated representations of plant hydraulics (Fang et al., 2022; Xu et al., 2023), wildfire (Thonicke et al., 2010; Li et al., 2012; Huang et al., 2020a; Huang et al., 2021), soil biogeochemistry and nutrient cycling (Li et al., 1992; Parton et al., 1988; Jenkinson, 1990), dynamic vegetation distributions (Martín Belda et al., 2022; Weng et al., 2015; Fisher et al., 2015; Liu et al., 2019), radiation-topography interaction (Hao et al., 2021), urban-scale processes (Oleson and Feddema, 2020; Krayenhoff et al., 2020), subsurface multiphase flow (Bisht et al., 2017; Qiu et al., 2024), and land use and management (Huang et al., 2020b; Binsted et al., 2022; Calvin et al., 2019). These improvements not only advance the capability of LSMs to model complex environmental interactions but also facilitate a mechanistic understanding of changes in land-atmosphere interactions under varying environmental conditions. Particularly, they can be used to predict the disturbance of the land surface, for example, Earth's ecosystem and surface hydrology, in response to climate change and to quantify the respective biogeophysical and biogeochemical feedbacks to the climate system (Ban-Weiss et al., 2011; Fisher and Koven, 2020).

75   Recent advancements in LSMs have broad applications in land-only simulations and within global

76   climate models (GCMs) to capture the complex interactions surrounding global climate change (Lawrence

77   et al., 2019; Martín Belda et al., 2022; Wiltshire et al., 2020). However, the application within GCMs does

78   not allow for the representation of land processes at kilometer scales and extreme events occurring at daily

79   to weekly scales (such as extreme precipitation and flash drought), which are more relevant to human

80   society. While regional refinement may appear to be a feasible solution, the associated computational costs

81   restrict their wide adoption within the weather and climate modeling community. Alternatively, combining

82   advanced LSMs with Regional Climate Models (RCMs) could facilitate more in-depth examinations of the

83   climate change impacts on land surfaces and the resulting feedback at scales that have greater relevance to

84   human society.

85   The U.S. Department of Energy's Energy Exascale Earth System Model (E3SM) Land Model

86   (ELM) is an advanced LSM that simulates the exchanges between terrestrial land surfaces and other Earth

87   system components, enabling us to understand hydrologic cycles, biogeophysics, and the dynamics of

88   terrestrial ecosystems (Burrows et al., 2020). The Weather Research and Forecasting (WRF) model serves

89   as an essential tool widely used for regional weather prediction and climate change analysis (Skamarock

90   and Klemp, 2008). WRF can be run with various LSMs such as Noah, Noah-MP, SSiB, CLM4. It has also

91   been coupled with CTSM recently (CTSM Development Team, 2024; Ucar, 2020). However, integrating

92   ELM with WRF enables comprehensive representation of land processes, following recent advancements

93   in ELM, for more computationally efficient regional modeling applications. For instance, leaf to canopy

94   upscaling through a two-big-leaf parameterization in ELM enables simulation of the diffuse radiation

95   fertilization effect (Chakraborty et al., 2022a), and thus better estimates of surface water and carbon budget,

96   a feature not present in Noah. As another example, ELM incorporates gridwise surface properties such as

97   leaf area index (LAI), displacement height, and vegetation top and bottom height. In contrast, Noah and its

98   variants use lookup tables with these properties prescribed for each land cover class, limiting their ability

99   to capture spatial heterogeneity in surface properties within individual land cover types. Moreover, ELM

100   simulations at ~km resolution highlight the significance of considering radiation-topography interaction in

101   simulating surface energy balance and water budget, a process not yet considered by current land models

102   in WRF (Hao et al., 2021; Yuan et al., 2023).

103   This study integrates ELM v2.1 with WRF (hereafter named WRF-ELM) using a modified coupler

104   derived from University Corporation for Atmospheric Research (UCAR)'s Lightweight Infrastructure for

105   Land-Atmosphere Coupling (LILAC) (Ucar, 2020). We evaluate the model performance using a broad

106   range of site observations and reanalysis data, providing a benchmark for subsequent model enhancements.

107   This effort expands the capability of a global LSM, which has been previously used within GCM

108   frameworks, allowing it to simulate higher resolution land-atmosphere interactions at regional scales. The

109   introduction and release of WRF-ELM also benefit the ELM user community by providing opportunities

110   for them to test new land schemes with atmospheric feedbacks and calibrate model parameters in coupled

111   models.

112

113   **2. Methods**

114   **2.1 Coupler in E3SM**
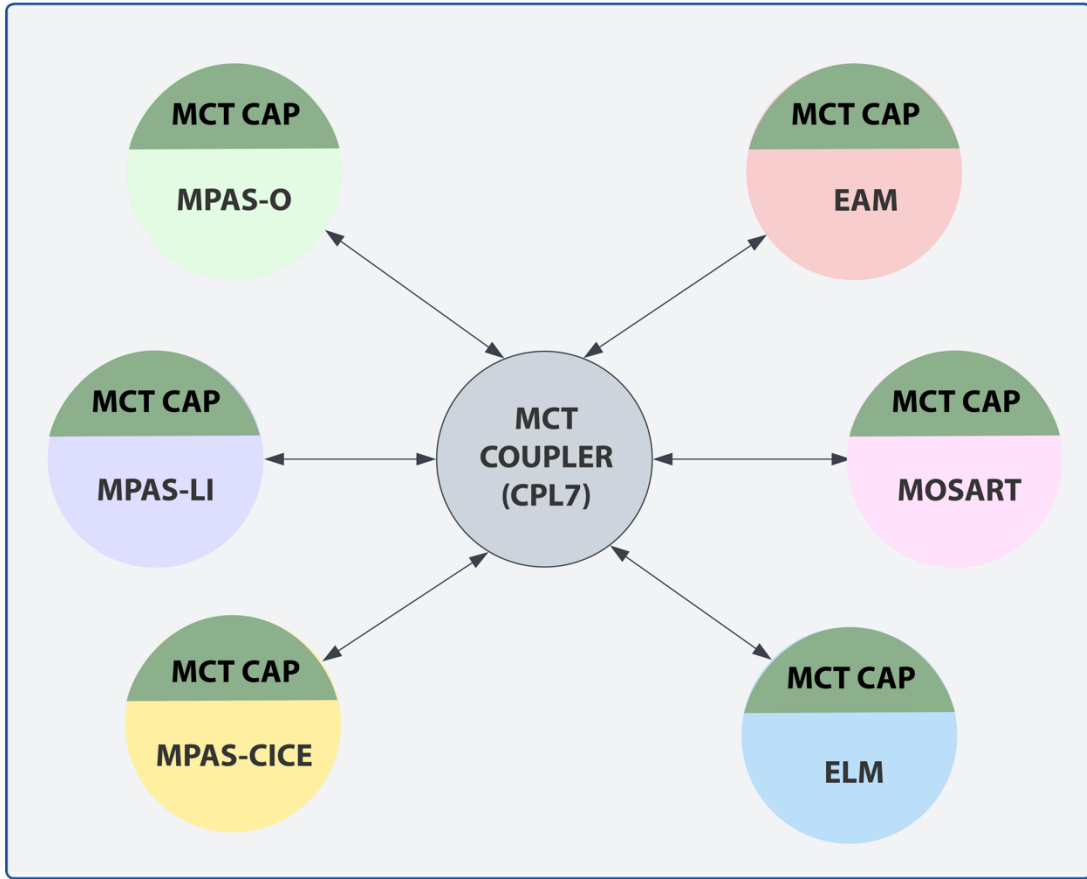
115

Short Name	Full Name
ELM	Energy Exascale Land Model
EAM	Energy Exascale Atmosphere Model
MOSART	Model for Scale Adaptive River Transport
MPAS-O	Model for Prediction Across Scales – Ocean
MPAS-CICE	Model for Prediction Across Scales – Sea Ice
MPAS-LI	Model for Prediction Across Scales – Land Ice

116 **Figure 1** Schematic diagram of the E3SM model components. The top-level coupler (CPL7) serves as the

117 main program for communication between each component. The Model Coupling Toolkit (MCT) cap in

118 each component provides an interface between CPL7 and the physical core, which is responsible for

119 memory allocation, preprocessing, post-processing, and input and output (I/O). The inserted table explains

120 the full names of all abbreviations in the figure.

121

122   E3SM adopts a hub-and-spoke architecture to couple the different model components together, as

123 shown in Figure 1. In this architecture, communication between the parallel components is realized via the

124   Model Coupling Toolkit (MCT; (Larson et al., 2005; Jacob et al., 2005)). The top-level coupler, version 7

125   coupler (CPL7), calls model component initialization, execution, and finalization methods through

126   specified interfaces (Craig et al., 2012). The MCT cap within each component provides an interface between

127   the CPL7 and the physical core, which is responsible for memory allocation, preprocessing, post-processing,

128   and input and output (I/O). Importantly, the inter-component communication is realized only through the

129   central hub, instead of direct communication with one another. The E3SM coupling framework imposes

130   strict requirements on how an atmospheric model can communicate with ELM. One particular challenge is

131   that many atmosphere models – including WRF – expect to run the land model in the middle of the time

132   step sequence. Accomplishing this in the E3SM architecture can require significant restructuring of the

133   atmosphere model. For this reason, ELM has not been coupled to atmospheric models in the regional model

134   community, limiting its ability to address complex scientific challenges at fine resolutions.

135

136   **2.2 LILAC-ESMF Coupler**

137
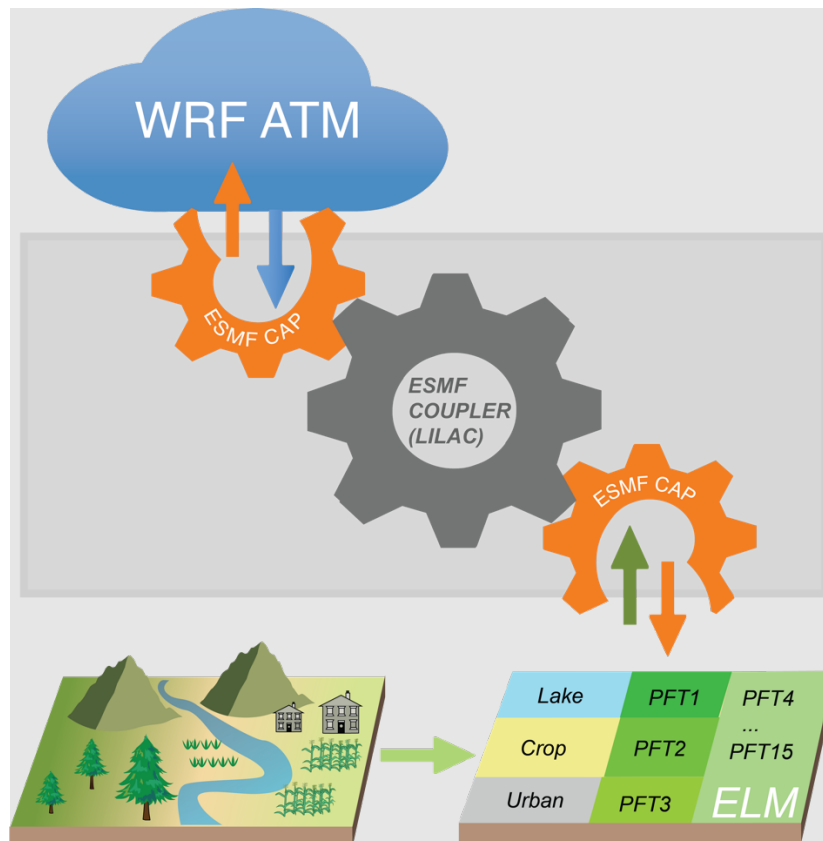
Figure 2 Schematic diagram of the coupling framework for WRF-ELM. The top-level coupler (LILAC) is in charge of communication between WRF ATM and ELM. The ESMF Cap within ELM and WRF ATM is responsible for memory allocation, preprocessing, post-processing, and input and output (I/O). PFT represents plant functional types in the figure)

The traditional way of coupling between LSMs (CLM4, Noah, Noah-MP, and SSiB) and WRF is through internal subroutines and interfaces within the WRF codebase. This tight coupling means that the LSM is often compiled and run as an integral part of the WRF model. As the LSMs grow to integrate more land processes, the tight coupling approach can become less scalable and harder to manage. Additionally, maintaining the coupled system updated with the latest versions of WRF and LSMs can be challenging due to the need for synchronized updates and compatibility checks. In contrast, modern approaches such as LILAC-ESMF offer a more modular and flexible way of coupling, facilitating easier integration and updates of different model components.

We have developed an ESMF (Hill et al., 2004) Cap which wraps ELM to facilitate seamless communication with the central hub driver that connects WRF ATM and ELM (Fig. 2). The central hub driver, LILAC, is developed using ESMF and provides the fundamental functions to support the integration of an LSM within an RCM, including 1) creating the list of fields passed from WRF ATM to ELM and vice versa; 2) initializing ESMF Caps for WRF ATM and for ELM); 3) coordinating calls of the ESMF Caps and ELM and exchanging data between these components; and 4) providing missing atmospheric fields, specifically for atmospheric aerosols

Within the coupling framework, the ESMF Cap provides the functions of 1) converting the input data from LILAC to the land model and vice versa; 2) supplying any additional input fields that ELM requires but are not provided by WRF ATM, for example, gross domestic product, population density, and lightning that are used to predict fire ignitions in ELM; and 3) setting the domain decomposition and generating the land mesh. The ESMF cap, which provides the necessary infrastructure to connect LILAC and ELM physics, serve as an example for similar coupling work between other LSMs and RCMs.

164

2.3 Exchange variables between WRF and ELM

ELM is driven by meteorological forcings including precipitation, downward shortwave radiation, downward longwave radiation, zonal wind at reference height (z_{atm}), meridional wind at z_{atm}, pressure at z_{atm}, specific humidity at z_{atm}, and air temperature at z_{atm}. In the coupled version, the meteorological forcings are provided by WRF ATM with the ELM model timestep set to match the integration timestep in the WRF ATM. The reference height refers to the height of the lowest atmosphere model level. The radiation scheme in WRF further splits the shortwave radiation to direct and diffuse components, as well as visible and near-infrared radiation. Precipitation is divided into rainfall and snowfall based on the frozen precipitation ratio, which are then inputted into the ELM. The ELM output includes skin temperature, 2-m air temperature, 2-m specific humidity at the surface, friction velocity, surface albedo, sensible heat flux, latent heat flux, ground heat flux, surface emissivity, and roughness length for momentum and heat transfer, which will be exchanged with the WRF ATM component.

177

2.4 Mesh data and surface parameters

In addition, mesh data is used in the WRF ATM to define the latitude and longitude of the grid. The domain information is necessary for the coupler and the land model during runtime. These data include a mask that informs the land model where to run and a land fraction that the coupler uses to combine fluxes from various surface types over a grid cell. The surface data configures the spatially implicit features (e.g., spatial fraction coverage, leaf and soil albedo, leaf and soil emissivity, etc.) of subgrid elements within grid cells (topographic unit, land cover, soil columns, and vegetation).

While a regular latitude/longitude grid is widely used for domain and surface data in the land-only mode, when coupled with WRF ATM, ELM needs to adopt the Lambert Conformal projection used in WRF. To create a domain file of Lambert Conformal projection, a grid descriptor file based on the WRF Pre-Processing System (WPS) output (e.g., geo_em.d01) needs to be created, which is then used to create the domain file used in ELM. A similar workflow is needed for surface data, which contains a large number of

190 input files that need to be interpolated by the land model. To generate both domain files and surface data, we

191 employ the ELM preprocessing tools that derive the input data and grid descriptor files for each dataset,

192 produce mapping files from the input data grid to our target grid, and then use the mapping weight files for

193 interpolation.

194

195 **2.5 Parallelization**
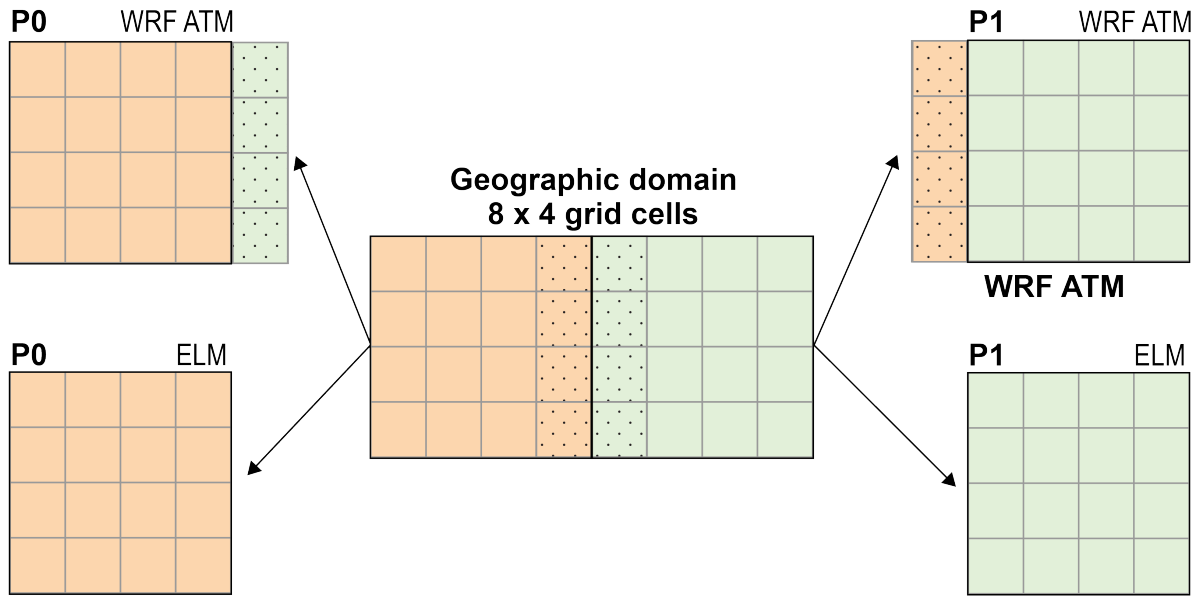
196

197 **Figure 3** Schematic of parallel domain decomposition scheme in WRF-ELM. The dotted area indicates

198 'halo' arrays in which memory is shared between processors (P0 and P1). WRF ATM and ELM are

199 calculated under the same processor.

200

201 Instead of adopting ELM's native round-robin domain decomposition strategy, our parallelization

202 strategy for WRF-ELM is to use geographic domain decomposition, as in WRF ATM. As shown in Fig. 3,

203 different grid cells in the model's physical domain are running on separate processors pre-assigned by the

204 user. On each processor, ELM within WRF employs parallel I/O to read atmospheric forcings, uses the

205 surface properties and land-use datasets to configure individual land cells, and then conducts massively

206   parallel simulations over these grid cells within each subdomain independently. In WRF ATM, the 'halo'

207   arrays share memory between processors, and message passing between processors is accomplished using

208   the message passing interface (MPI; (Gropp et al., 1996)).

209

210   **3. Model Validation**

211   **3.1 WRF-ELM configuration**

212   For our first WRF-ELM application, we study the land-atmosphere interactions over the Great

213   Lakes Region (GLR), a hydrodynamically complex and heavily populated region with both natural surface

214   heterogeneity and significant land management practices. This domain also includes the world's largest

215   freshwater system, comprising of Superior, Michigan, Huron, Erie, and Ontario Lakes. This region is the

216   focus of the U.S. Department of Energy's (DOE's) Coastal Observations, Mechanisms, and Predictions

217   Across Systems and Scales, Great Lakes Modeling (COMPASS-GLM) project, which has an overall goal

218   of developing a fully coupled (lake-land-atmosphere) regional earth system model centered on the GLR

219   (Kayastha et al., 2023). Here, we report the initial implementation of the WRF-ELM framework to support

220   its ability to capture atmospheric, coastal, urban, and rural interactions, providing a baseline reference

221   solution for further model development.
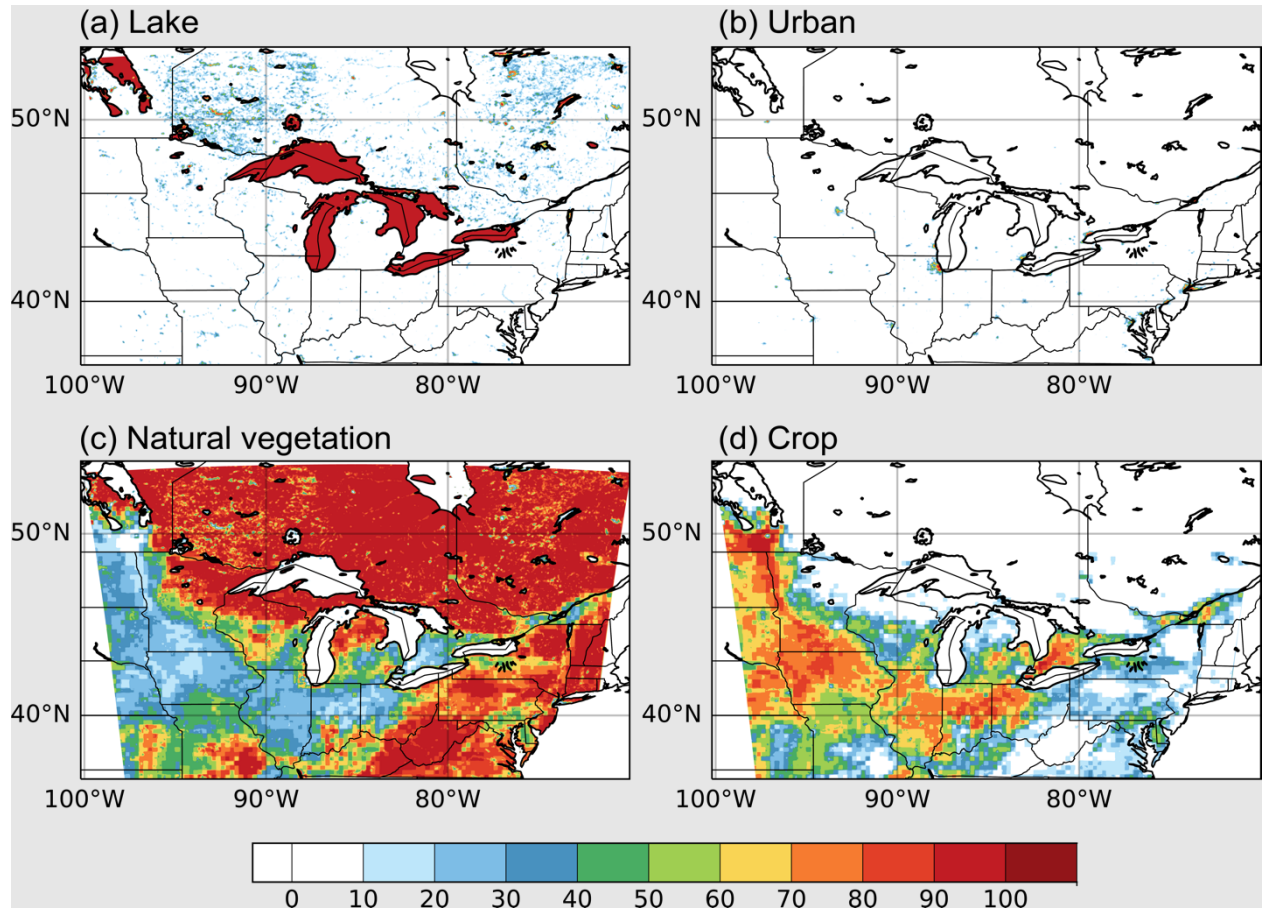
Figure 4 Fractional coverage (%) of major land unit (a) lake, (b) urban, (c) natural vegetation, and (d) crop used in the WRF-ELM.

The RCM used in the numerical simulation is based on the WRF model version 4.4.2 with the Advanced Research WRF dynamic core (Skamarock and Klemp, 2008). Following Wang et al. (2022a), the model domain is centered at 45.5°N and 85.0°W and has dimensions of 544 × 485 grid points in the west–east and south–north directions. The simulation domain covers the GLR, with a spatial resolution of 4 km (Fig. 4). Fifty vertical layers from the surface to 50 hPa are adopted with denser layers at lower altitudes to sufficiently resolve the PBL. We conduct 5 ensemble members in 2018, starting with initial conditions 12 hr apart between 0000 UTC on 12 May and 0000 UTC on 14 May and ending on 0000 UTC 1 September 2018. The resulting simulations are analyzed during June, July, and August (JJA) 2018.

Table 1 Model Configuration in WRF and ELM.

WRF specific options and schemes	
Meteorological IC/LBCs	ERA5
Microphysics	Thompson microphysics
Radiation	RRTMG for longwave and shortwave
Land surface	ELM or CTSM
Planetary boundary layer	YSU scheme
Lake surface temperature	NOAA GLSEA
ELM/CTSM input data	
Land use and land cover	ELM/CTSM default parameter
Vegetation	ELM/CTSM default parameter
Soil color	ELM/CTSM default parameter
topography	ELM/CTSM default parameter
Number of plant functional types (PFT)	16

235

236   The meteorological initial condition (IC) and lateral boundary conditions (LBCs) have been derived

237   from the ECMWF Reanalysis v5 (ERA5; (Hersbach et al., 2020)) at 0.25° horizontal resolution and 3-hour

238   temporal intervals (Table 1). The WRF model incorporates the Thompson microphysics (Thompson et al.,

239   2004; Thompson et al., 2008), the Rapid Radiative Transfer Model for GCMs longwave and shortwave

240   schemes (Iacono et al., 2008), and the Yonsei University planetary boundary layer scheme (Hong and Lim,

241   2006). We turn off cumulus parameterization, considering the convection-permitting resolution of the

242   ensemble simulations. The lake skin temperature is obtained from NOAA Great Lakes Surface

243   Environmental Analysis (GLSEA) data set (Schwab et al., 1992) derived from Advanced Very High-

244   Resolution Radiometer.

245   For the land surface model, we adopt ELM with satellite phenology (ELM-SP) mode which utilizes

246   seasonal varying leaf area index prescribed based on the MODIS data. The default ELM land surface

247   parameters have been used in the coupled model simulation, including land use and land cover information,

248   vegetation biogeophysical properties, soil properties, and topography. The surface parameter is also

249   applicable in CTSM (Table 1). A detailed description of ELM/CTSM default parameter can be found in (Li

250   et al., 2024). The current version of WRF-ELM does not enable biogeochemistry (ELM-BGC) mode and

251   thus does not simulate carbon and nitrogen cycles. In addition, we also conduct simulations using the WRF

252   coupled with Community Terrestrial Systems Model (CTSM ctsm5.1.dev114) (Lawrence et al., 2019)

253   (WRF-CTSM hereafter), which can be used to compared with WRF-ELM's performance in capturing the

254   land-atmosphere exchanges of energy and water fluxes. CTSM is also referred to the community land model

255   version 5 (CLM5) afterwards. We emphasize that the comparison against WRF-CTSM is not intended to

256   demonstrate the superior performance of WRF-ELM but to show that the newly developed WRF-ELM

257   performs comparably well to WRF-CTSM, one of the most advanced and sophisticated land surface models.

258
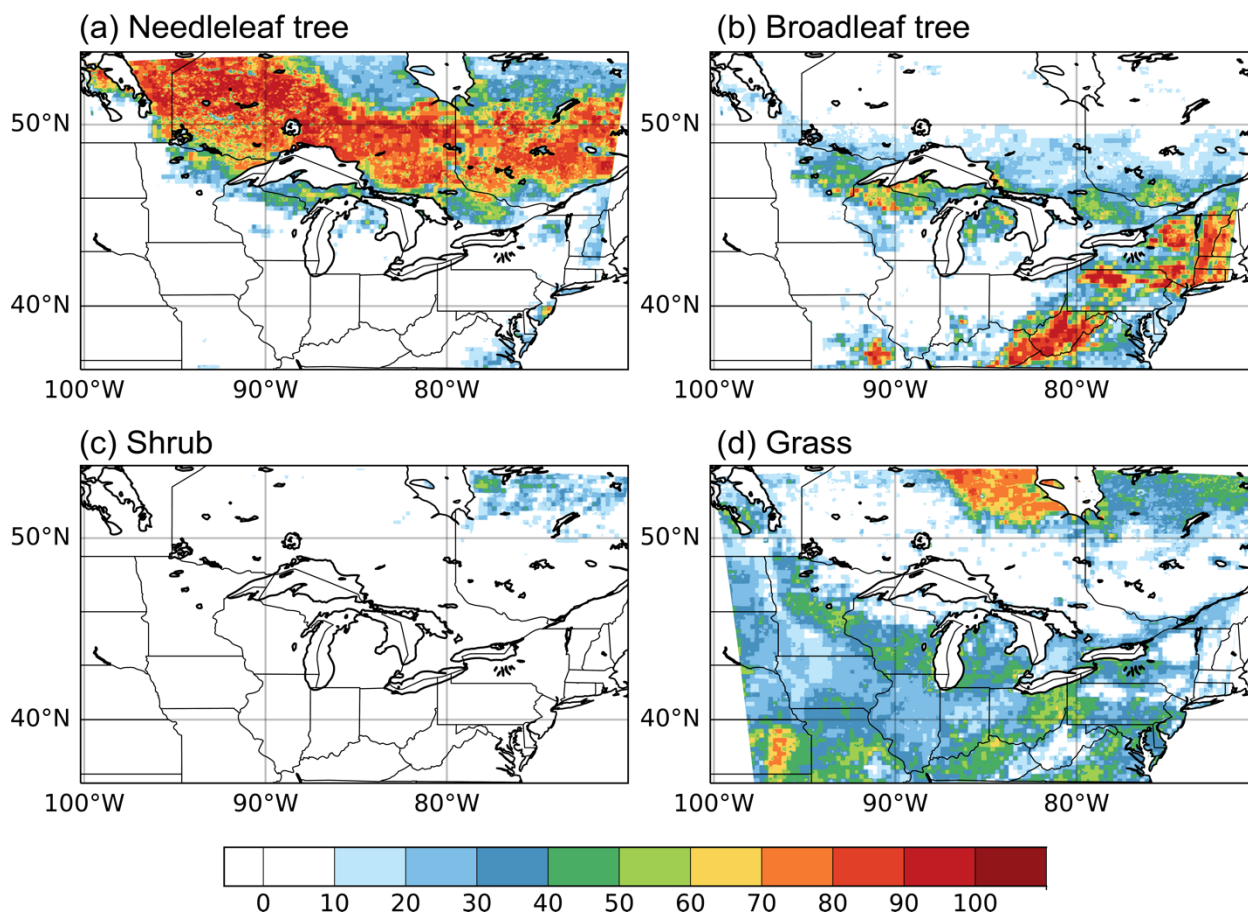
259

260   **Figure 5** Fractional coverage (%) of major plant functional types (a) needleleaf forest (deciduous and

261   evergreen combined), (b) broadleaf forest (deciduous and evergreen combined), (c) shrub, and (d) grass

262   used in the WRF-ELM.

263

264   It is noteworthy that there are several distinctions between WRF-ELM and the version of WRF-

265   CTSM we use here. WRF-CTSM aims for a relatively fast calculation speed, thus it has simplified the

266 description of land cover and kept the single dominant land unit and single dominant plant functional types

267 (PFTs). In our simulation region, WRF-CTSM identifies the Great Lakes in the center of the simulation

268 domain, with the natural vegetation prevailing in the northern and southeastern regions, and crops

269 dominating the southwestern areas (Fig. 4). On the other hand, WRF-ELM preserves the comprehensive

270 description of subgrid heterogeneity. As a result, the fluxes calculated from various surface types are

271 merged using a weighted-average method before transferring to the upper-level WRF ATM. This is

272 particularly important in regions with mixed vegetation types, such as the southwestern part of our study

273 domain. Moreover, within the natural vegetation land unit, WRF-ELM simulates the blend of needleleaf

274 and broadleaf trees (evergreen and deciduous combined) around the Great Lakes and the mixture of crops

275 and grasses in the southwestern part of the domain (Fig. 5).

276

277 **3.2 Data for validation**

278

Table 2 Dataset for validation in the study.

Dataset	Variables	Spatial resolution	Temporal resolution	Reference
ASOS	Air temperature at 2-m, Dew point	point	Hourly	(Nadolski, 1992)
AmeriFlux	Latent heat, Sensible heat	point	Hourly	(Law, 2005)
Daymet	Maximum air temperature at 2-m, Maximum air temperature at 2-m, Precipitation	1 km	Monthly	(Thornton et al., 2022)
NLDAS	Air temperature at 2-m, Precipitation	0.125 °	Monthly	(Xia et al., 2012)
ERA5-Land	Air temperature at 2-m, , Latent heat, Sensible heat	9 km	Monthly	(Muñoz-Sabater et al., 2021)
NCEP Stage IV	Precipitation	4 km	Monthly	(Lin and Mitchell, 2005)

279

280   Observational and reanalysis data from multiple sources have been used to evaluate WRF

281   simulation results (Table 2). We select 12 paired sites from the Automated Surface Observing System

282   (ASOS) to acquire 5-minute 2-meter air temperature (Ta) and 2-meter dew point temperature over the urban

283   and rural area in the GLR (https://www.ncei.noaa.gov; last accessed: November 2023). The 2-meter relative

284   humidity (RH) is derived from Ta and dew point. We compute hourly averages of Ta and RH from the 5-

285   minute data to match the hourly WRF outputs.

286

287   **Table 3** AmeriFlux site information (LCF: land cover type; DBF: deciduous broadleaf tree; MF: mixed

288   forest; NEON: National Ecological Observatory Network)

Site ID	Latitude	Longitude	LCF	PI(s)	DOI
US-xST	45.5089	-89.5864	DBF	NEON	https://doi.org/10.17190/AMF/1617737
US-xTR	45.4937	-89.5857	DBF	NEON	https://doi.org/10.17190/AMF/1634886
US-WCr	45.8059	-90.0799	DBF	Ankur Desai	https://doi.org/10.17190/AMF/1246111
US-xUN	46.2339	-89.5373	MF	NEON	https://doi.org/10.17190/AMF/1617741
US-PFa	45.9459	-90.2723	MF	Ankur Desai	https://doi.org/10.17190/AMF/1246090
US-Syv	46.242	-89.3477	MF	Ankur Desai	https://doi.org/10.17190/AMF/1246106

289

290   In addition, we collect measurements of latent heat (LH) and sensible heat (SH) from six flux tower

291   sites provided by AmeriFlux (http://ameriflux.lbl.gov; last accessed: November 2023). Initially, 16

292   AmeriFlux sites have been selected within our study domain for the JJA 2018 period, which included

293   measurements over grassland, mixed forest, and deciduous broadleaf forest. However, ten sites are filtered

294   out because their land cover types differ from the dominant ones used in WRF-CTSM. The latitudes and

295   longitudes of selected sites have been documented in Table 3. The hourly LH and SH data from AmeriFlux

296   have been reduced to daily averages to validate the model simulation of surface energy fluxes.

297   We also acquire reanalysis datasets to evaluate the model performance in simulating the climate

298   variables and energy fluxes. All datasets are resampled using bilinear interpolation to a 4 km resolution to

align with the WRF grids. We employ the Daymet dataset from https://daymet.ornl.gov (last accessed:

October 2023), which provides daily, gridded (1 km × 1 km) estimates of solar radiation, 2-meter maximum

(Tmax) and minimum (Tmin) temperature, precipitation (PRE), snow water equivalent, and water vapor

across the CONUS (Thornton et al., 2022). It uses local regression algorithms to interpolate and extrapolate

daily meteorological observations from Global Historical Climatology Network (GHCN). Daymet

considers the effects of elevation on climate and generates daily meteorological variables for a particular

grid cell using the weighted linear regression-based approach. We download monthly Tmax, Tmin, and

precipitation from Daymet version 4.5, and average the temperatures to compare against model simulated

daily mean Ta.

Monthly Ta from the North American Land Data Assimilation System version 2 (NLDAS) with

Noah LSM is used as an additional source of reanalysis data to evaluate WRF-ELM. These data are

available beginning in 1979 at a 0.125° resolution (Xia et al., 2012). NLDAS constructed a forcing dataset

from a daily gauge-based precipitation analysis, bias-corrected shortwave radiation, and surface

meteorology reanalyses from North American Regional Reanalysis (NARR) to drive four different LSMs

to derive surface fluxes and state variables. We acquire the product derived using the Noah model

(https://disc.gsfc.nasa.gov; last accessed: October 2023) because it is one of the most commonly used LSMs

and has been frequently coupled with climate and atmospheric models.

The ERA5-Land reanalysis provides surface variables at the 0.1° x 0.1° resolution (Muñoz-Sabater,

2019). The data are produced under the offline mode forced by meteorological fields from ERA5 (Muñoz-

Sabater et al., 2021), without coupling to the atmospheric module of the ECMWF's Integrated Forecasting

System. ERA5-Land datasets have also been widely used for a variety of land condition assessments (Pelosi

et al., 2020; Stefanidis et al., 2021; Wang et al., 2022b). We acquire monthly Ta, SH, and LH in ERA5-

Land from Google Earth Engine (collection ECMWF/ERA5_LAND/MONTHLY_AGGR; last accessed:

October 2023).

Lastly, we acquire precipitation data from the National Centers for Environmental Prediction

(NCEP) Stage IV dataset (Lin and Mitchell, 2005), a gridded product with 4 km spatial and hourly temporal

325   resolution that covers the period from 2002 to the present. NCEP compiles the Stage IV product using data

326   from 140 radars and approximately 5,500 gauges across the CONUS. Stage IV provides highly accurate

327   precipitation estimates, particularly for medium to heavy precipitation, and has therefore been widely used

328   as a reference for precipitation evaluation (Nelson et al., 2016).

329

330   **3.3 Results**

331   **3.3.1 Temperature**
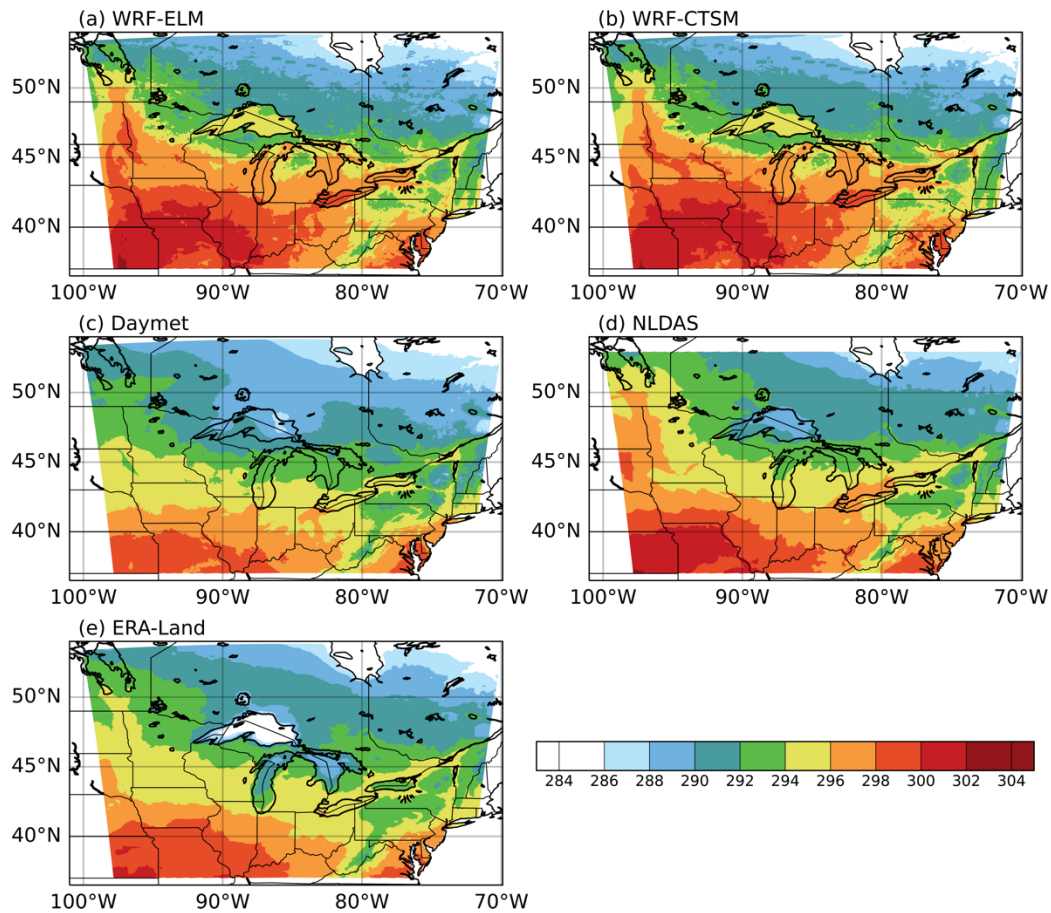
332

333   **Figure 6** June-July-August mean 2-m air temperature (K) in (a) WRF-ELM, (b) WRF-CTSM, (c) Daymet,

334   (d) NLDAS, and (e) ERA-Land. The numbers on the top right of (c)-(f) indicate the spatial correlation

335   coefficient between each reanalysis product and the two simulation results.

336

337 **Table 4** Evaluation metrics of June-July-August 2-m air temperature between each model result and the

338 reanalysis product. CORR: spatial correlation coefficient; RMSE: Root mean square error.

		Daymet	NLDAS	ERA-Land
	Bias	1.70	0.34	1.20
WRF-ELM	CORR	0.94	0.94	0.86
	RMSE	2.18	1.43	2.30
	Bias	1.79	0.43	1.29
WRF-CTSM	CORR	0.94	0.93	0.86
	RMSE	2.30	1.57	2.40

339
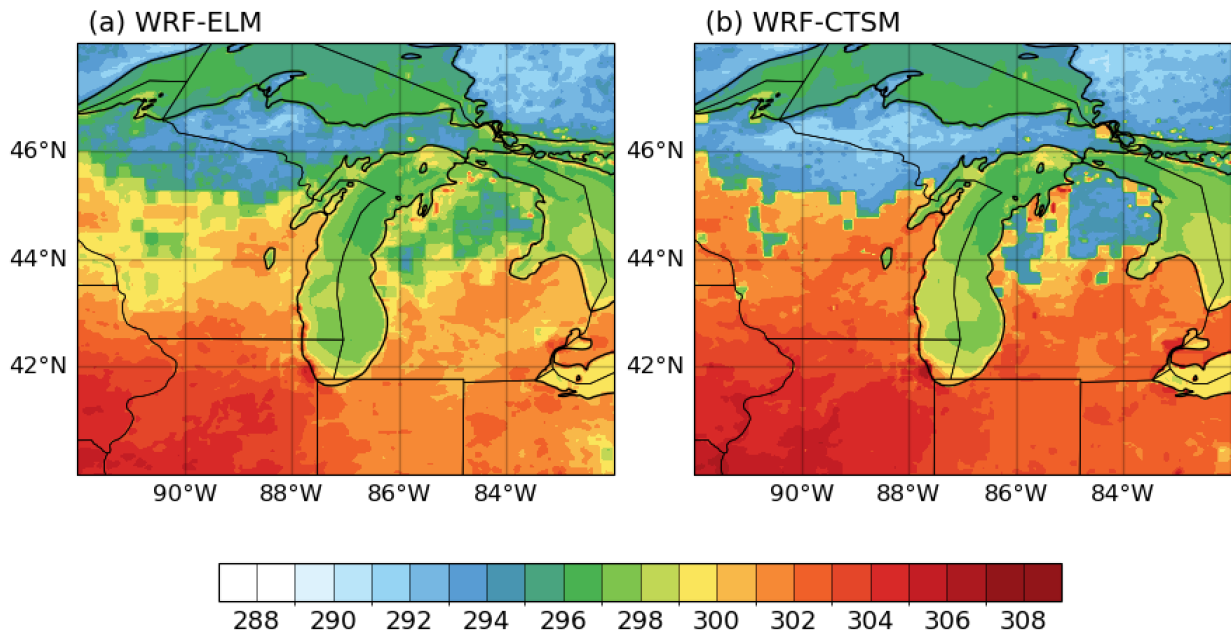
340

341 **Figure 7** June-July-August mean skin temperature (K) in (a) WRF-ELM, (b) WRF-CTSM, zoomed-in view

342 focuses on the area surrounding Lake Michigan

343

344   The spatial distribution of Ta from the WRF-ELM and WRF-CTSM models, along with reanalysis

345 data such as Daymet, NLDAS, and ERA5-Land, is illustrated in Figure 6. Both WRF-ELM and WRF-

346 CTSM have reasonably captured the spatial pattern observed in the reanalysis datasets, demonstrating a

347 spatial correlation coefficient (CORR) ranging from 0.86 to 0.95 (Table 4). The highest CORR is observed

348 with Daymet, while the lowest one is with ERA5-Land. Both models exhibit a warm bias compared to

349   reanalysis products. However, WRF-ELM shows a slightly lower bias and RMSE compared with WRF-

350   CTSM (Table 4). Additionally, WRF-ELM displays a smoother gradient in comparison to WRF-CTSM,

351   particularly over the GLR where needleleaf trees, broadleaf trees, grasses, and croplands coexist (Fig. 7).
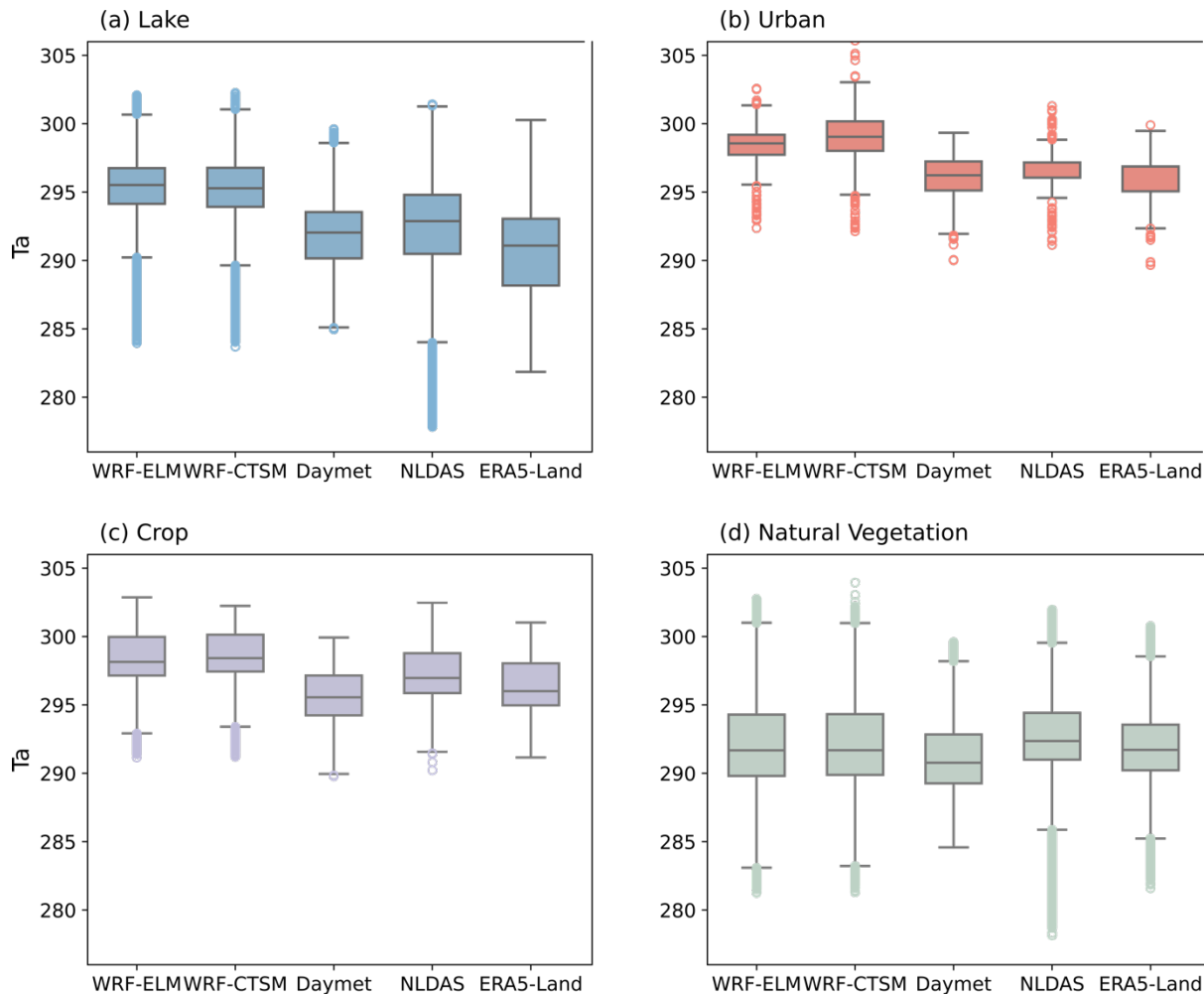
352

353   **Figure 8** Boxplots of June-July-August 2-m air temperature (K) over (a) lake, (b) urban, (c) crop, and (d)

354   natural vegetation in simulations and reanalysis products.

355

356   **Table 5** June-July-August 2-m air temperature over each land unit in simulations and reanalyses.

	WRF-ELM	WRF-CTSM	Daymet	NLDAS	ERA5-Land
Lake	295.5	295.4	292.1	292.3	290.6

Urban	298.5	299.0	296.2	296.7	296.0
Crop	298.4	298.6	295.8	297.4	296.5
Natural Vegetation	292.6	292.6	291.7	292.9	292.4

357

358   Despite the overall good performance of model simulation of Ta, it is slightly different among

359 different land units (Fig. 8). The largest warm bias is found over the lake surface, in which both models

360 have overestimated Ta by 3-5 K (Table 5, Fig. 8). For urban and crop areas, the WRF-ELM and WRF-

361 CTSM show a slightly warmer temperature by 2-3 K than all reanalysis data, which makes sense since

362 reanalysis datasets do not capture urban-scale warming signals (Chen et al., 2024). The Ta over the natural

363 vegetation is well captured, with the average value in both models within the range of average Ta over all

364 datasets.

365
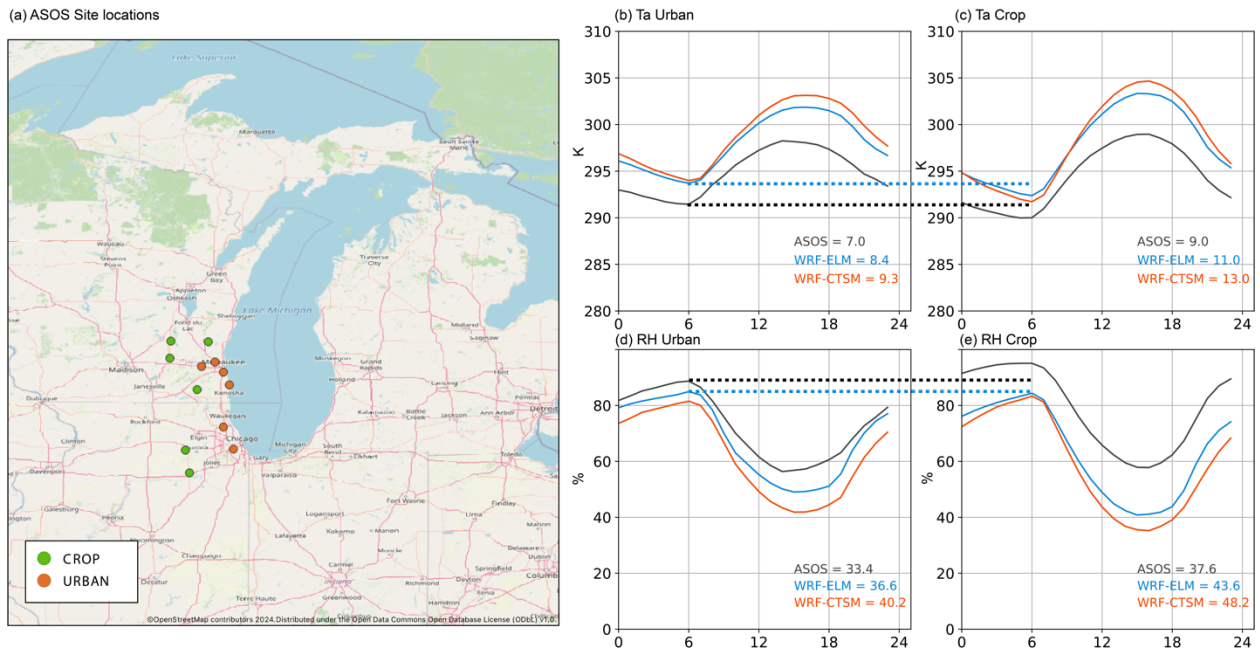
366 **Figure 9** (a) The location of ASOS sites. (b-c) June-July-August averaged hourly 2-meter air temperature

367 over (b) urban and (c) crop land units for ASOS, WRF-ELM, and WRF-CTSM. (d-e) The same as (b-c) but

368 for 2-meter relative humidity. The numbers in (b-e) indicate the diurnal ranges of air temperature and

369 relative humidity from ASOS, WRF-ELM, and WRF-CTSM. The dash lines highlight the nighttime Ta and

370 RH when urban and crop contrasts are significant.

371

372   We use ASOS sites to investigate the representation of urban and lake effects on air temperature

373 and relative humidity over the metropolitan area, emphasizing the interaction between the urban heat island

374 (UHI; Rizwan et al., 2008) and lake breeze in WRF-ELM and WRF-CTSM. Six urban sites along the west

375 coast of Lake Michigan were selected, paired with six adjacent crop sites as reference points (Fig. 9a).

376 Compared to the rural crop sites, the urban sites exhibit higher minimum Ta during the night, as urban areas

377 retain more heat during the daytime and gradually release after sunset. During late morning to noon, the

378 lake breeze tends to cool urban air, resulting in a lower daily maximum Ta than observed in crop areas

379 (Wang et al., 2023). In the afternoon, urban sites show a more gradual decline in Ta compared to rural sites,

380 driven by the cumulative heating effect of solar radiation absorption and the heat release by urban materials

381 throughout the day (Soltani and Sharifi, 2017). This characteristic of urban areas leads to a smaller diurnal

382 temperature range of 7.0 K, compared to a 9.0 K range over crop sites (Figs. 9b-c). The UDI effect is also

383 evident in 2m RH observations from ASOS, with urban areas showing lower RH values at night (Figs. 9d-

384 e).

385   Both WRF-ELM and WRF-CTSM capture the warmer nighttime Ta due to the UHI effect and the

386 cooler daytime Ta caused by the lake breeze over urban sites, adequately reproducing the smaller diurnal

387 range. WRF simulations, particularly WRF-ELM, reasonably capture urban RH at night, but both models

388 underestimate RH over crop areas, so the UDI is not well captured in the simulations. Notably, WRF-ELM

389 generally exhibits smaller biases in both Ta and RH compared to WRF-CTSM (Fig. 9). However, both

390 models systematically overestimate T2 and underestimate RH in both urban and crop areas, suggesting a

391 persistent warm and dry bias need to be further investigated in the ELM and CTSM component.

392

393 **3.3.2 Energy fluxes**

394
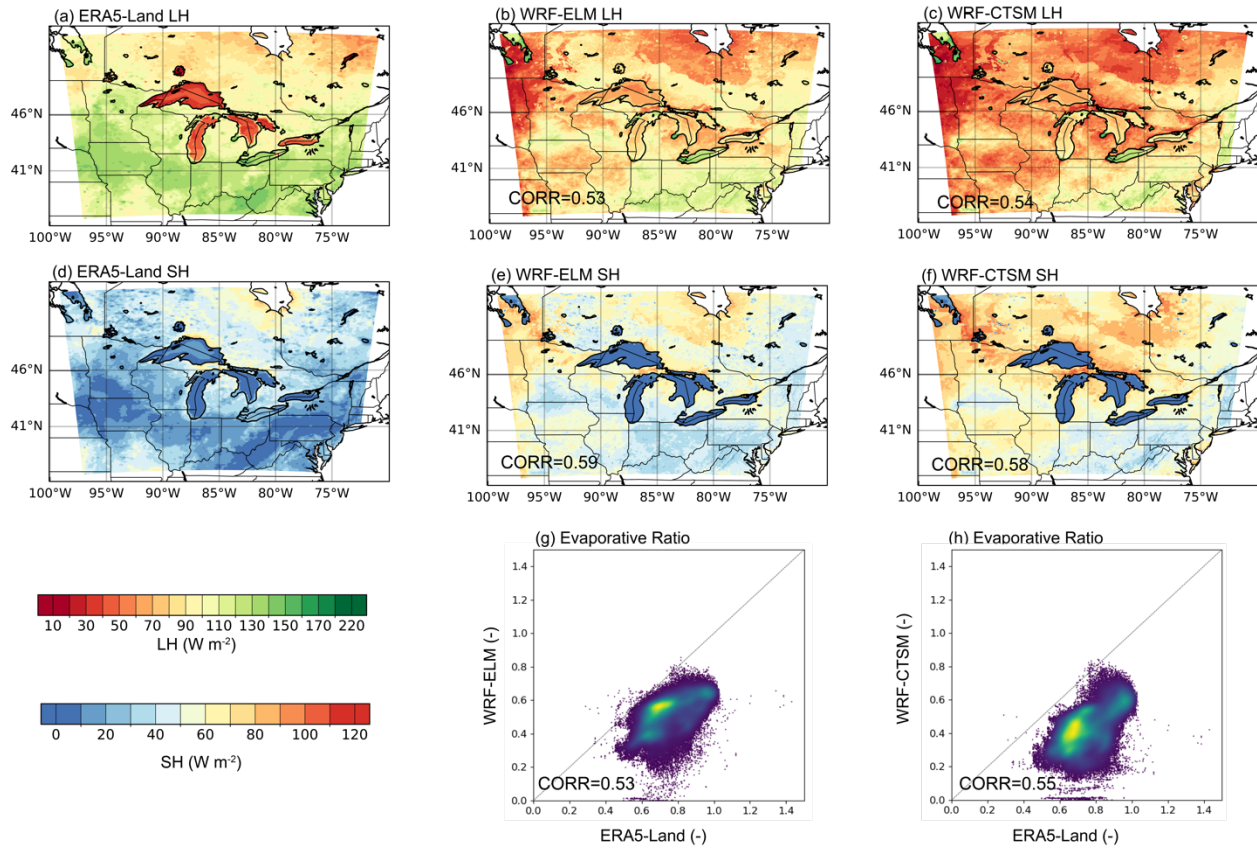
Figure 10 (a-c) Spatial distribution of latent heat in (a) ERA5-Land (b) WRF-ELM, and (c) WRF-CTSM;
(d-f) Spatial distribution of sensible heat in (d) ERA5-Land (e) WRF-ELM, and (f) WRF-CTSM; (g-h)
Comparison of evaporative ratio between (g) WRF-ELM and ERA5-Land and (h) WRF-CTSM and ERA5-
Land over the natural vegetation grids.
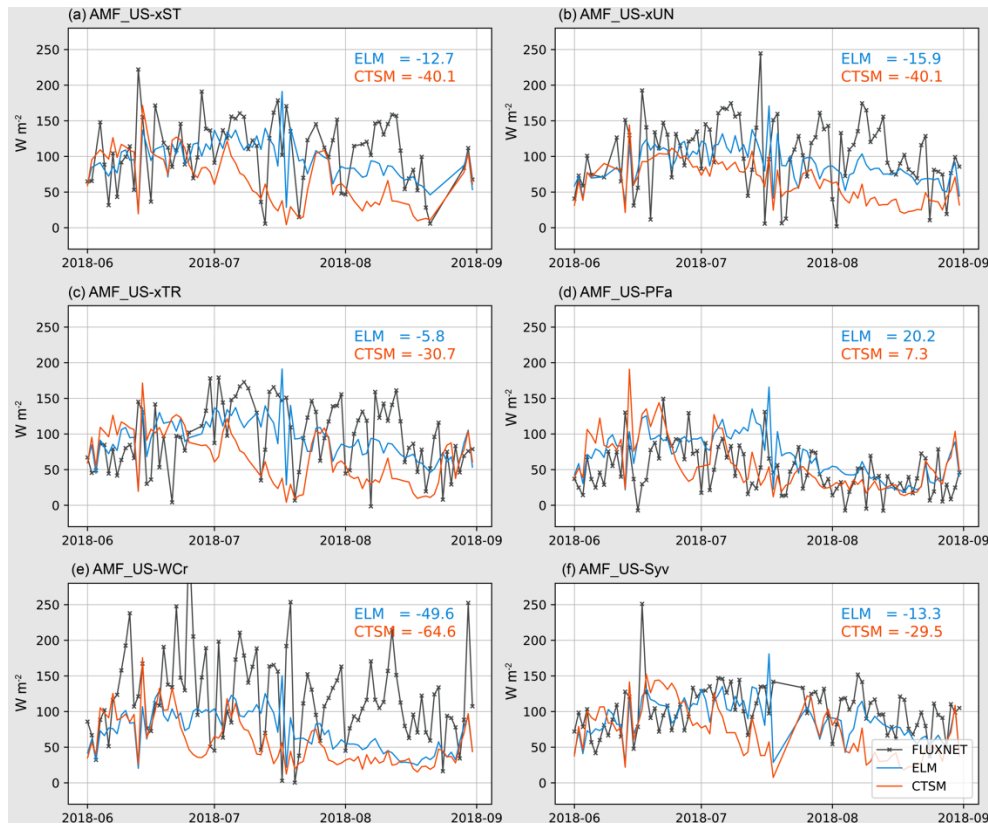
Figure 11 June-July-August averaged daily LH fluxes from six AmeriFlux sites and the corresponding model grids. The numbers indicate biases between WRF-ELM (or WRF-CTSM) and AmeriFlux.

We evaluated the simulated LH and SH fluxes from the WRF model simulations against ERA5-Land reanalysis data. The spatial correlation coefficients (CORR) range from 0.53 to 0.58 (Fig. 10a–f). Overall, both models capture the LH gradient across the study domain, with higher LH observed in the southern region and lower LH in the northern region. Similarly, both the reanalysis data and the models show a higher SH in the northern region and lower SH in the south. A systematic underestimation of LH (ranging between 22-35 W m^{-2}) and overestimation of SH (averaging 21-31 W m^{-2}) are evident in both WRF-ELM and WRF-CTSM. The observed evaporative fraction ranges from 0.6 to 0.8 in most vegetated grids; however, the corresponding simulated evaporative fraction is approximately 0.6. This evaluation further confirms that our models tend to underestimate LH fluxes while overestimating SH fluxes. These biases may be largely attributed to the surface parameters uncertainties used in the current simulations, such

414 as LAI or roughness length. These parameters have not been thoroughly calibrated in coupled E3SM

415 simulations focusing on the Great Lakes region.

416   A further comparison of daily LH values from six AmeriFlux sites over deciduous broadleaf forests

417 is illustrated in Fig. 11. WRF-ELM exhibits a smaller bias in reproducing the magnitude of LH than WRF-

418 CTSM; however, neither model captures the temporal variations well. Comparing regional model

419 simulations with site-level observations remains a consistent difficulty due to the inherent scale mismatch

420 between point observations and grid-based simulations. Additionally, since we examined a relatively short

421 period without interannual variability or seasonal cycles, the temporal variations of surface energy are

422 mostly related to the simulation of cloud and precipitation variations, which are among the most uncertain

423 parts of regional climate simulations.

424

425 **3.3.3 Precipitation**

426
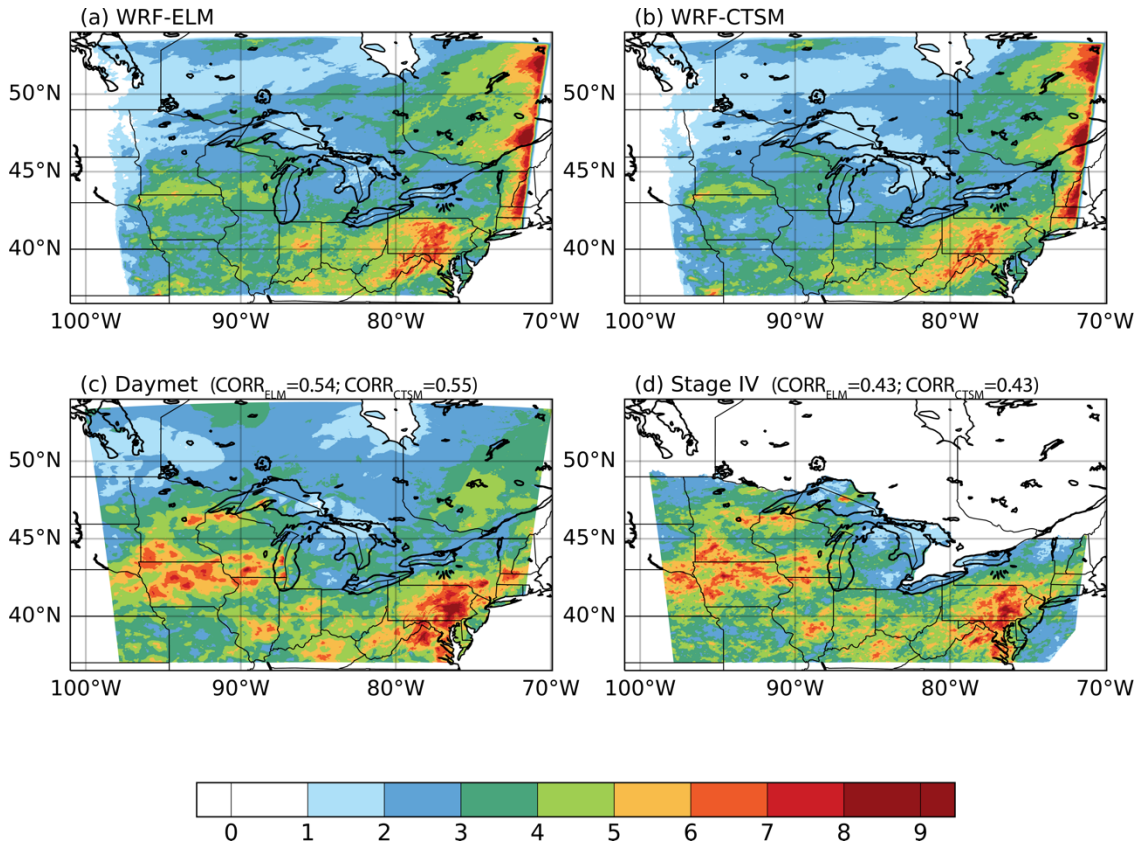
427

428 **Figure 12** The spatial distribution of June-July-August precipitation (mm d^{-1}) in (a) WRF-ELM, (b) WRF-

429 CTSM, (c) Daymet, and (d) ST4. The numbers on the top right of (c)-(d) indicate the CORR between each

430 observational product and the two simulation results.

431

432 Figure 12 presents the spatial distribution of precipitation from models and observations. It is

433 important to note that Stage IV primarily focuses on the CONUS region, while significant areas of our

434 simulation domain in Canada remain uncovered. Compared with the Daymet (PRE$_{Daymet}$ = 3.55 mm d^{-1}),

435 both WRF-ELM and WRF-CTSM capture the regional mean value (PRE$_{WRF-ELM}$ = 3.14 mm d^{-1} and PRE$_{WRF-}$

436 $_{CTSM}$ = 2.96 mm d^{-1}) and the spatial distribution of precipitation, exhibiting CORR ranging from 0.43 to 0.55.

437 The precipitation over the southeastern part of our study domain is well captured while that on the western

438 side of Lake Michigan is slightly underestimated, with WRF-ELM demonstrating a lower bias than WRF-

439 CTSM. This underestimation of precipitation aligns with the underestimation of latent heat and

440 evapotranspiration, suggesting that suppressed evapotranspiration may reduce moisture availability and

441 transport, particularly to the western GLR. Conversely, an overestimation of precipitation is evident along

442 the eastern boundary of our study domain.

443

444 **4. Discussion and Conclusions**

445 This study introduces a framework integrating the state-of-the-art land surface model, ELM, with

446 the widely used regional weather and climate model, WRF, named WRF-ELM. Moving beyond the

447 traditional way of coupling between LSMs and WRF through internal subroutines within the WRF codebase.

448 We adopt the LILAC-ESMF framework, a modular approach which maintains the integrity of the ELM's

449 source code structure and facilitates the transfer of future developments in ELM to WRF-ELM. After

450 coupling the two models, simulations using WRF-ELM have been conducted over the Great Lakes Region,

451 and their performance has been evaluated against observations and reanalysis data from multiple sources

452 and the WRF-CTSM simulations. These model simulations have been conducted at a resolution of 4 km ×

453 4 km, facilitating direct model validation and verification with various data sources. The use of seasonal

454 mean simulation outputs and diurnal cycles showcases the capabilities of WRF-ELM in representing the

455 temporal and spatial variations of water and energy cycles over the Great Lakes Region.

456 In general, our findings suggest that the newly coupled WRF-ELM effectively captures the spatial

457 distribution of surface state variables and fluxes across the GLR. The model displays a smoother gradient

458 in surface skin temperature than WRF-CTSM, due to the representation of sub-grid features within grid

459 cells. The model's performance is particularly reasonable over the natural vegetation, while a minor warm

460 bias is detected over crop and urban grids.

461 The slight overestimation of air temperature in crop regions could potentially be mitigated by

462 incorporating a more realistic representation of crops, such as crop rotation and irrigation. Additionally, the

463 application of spatially varying crop parameters closely captures the observed magnitude and seasonality

464 of carbon and energy fluxes compared to the observations (Sinha et al., 2023). However, these

465 improvements have only been tested using the land-only ELM. Our generalized coupling framework

466 supports future studies of sophisticated crop-atmosphere interactions at finer spatial resolution than those

467 achieved with coarse GCM simulations.

468 In addition, the UHI effects in cities surrounding the GLR are generally captured in both WRF-

469 ELM and WRF-CTSM, as indicated by the warmer night temperature in the cities. While there is an

470 overestimation of UHI compared to ASOS, this could be due to the simplified urban representation in ELM.

471 For instance, the urban surface emissivity in CLM, and thus ELM due to the shared model structure, is

472 reported to be noticeably lower than the values derived from satellites, resulting in a surface UHI effect that

473 is significantly higher than satellite-derived values (Chakraborty et al., 2021). Another potential

474 contributing factor could be the lack of representation of urban vegetation. The presence of vegetation tends

475 to mitigate the UHI effect (Paschalis et al., 2021) , and its absence in the urban subgrid would lead to an

476 overestimation of UHI values, all else remaining equal.

477 Our research develops the WRF-ELM framework and provides the first assessment of its

478 capabilities through high-resolution model simulations that fully capture expected patterns of land-

479 atmosphere interactions. Based on the validation and assessment of WRF-ELM results, this study delivers

480   a baseline reference, identifies common model biases in high-resolution regional applications, and proposes

481   pathways for subsequent model development for ELM, as well as the coupled model. The coupled model

482   provides an opportunity to investigate the impact of more sophisticated land processes, such as plant

483   hydraulics, dynamic vegetation distributions, and soil biogeochemistry, on weather and climate predictions.

484

485   **Author contributions:** HH designed the study, implemented the parameterization, performed the

486   simulations, analyzed the results, and drafted the original paper. YQ designed the study, discussed the results,

487   and edited the paper. GB, TT, BS, YL, and WS helped with the coupling design. JW, TT, DH, JL, ZY, PX,

488   EC and RH discussed the results and edited the paper.

489

490   **Code Availability:** The description and codes of E3SM v2.1 (including ELM v2.1) are publicly available

491   at   https://doi.org/10.11578/E3SM/dc.20230110.5   and   https://github.com/E3SM-

492   Project/E3SM/releases/tag/v2.1.0 (last access: 12 May 2023), respectively. Starting from ELM 2.1, the

493   model   codes   for   WRF-ELM   coupling   described   in   this   paper   are   available   at

494   https://github.com/hhllbao93/ELM and https://doi.org/10.5281/zenodo.11289807 (Huang, 2024).

495

496   **Competing interests:** At least one of the (co-)authors is a member of the editorial board of Geoscientific

497   Model Development.

498

499   **Acknowledgement**: The authors acknowledge the CTSM developer teams for making the LILAC release

500   available including Mariana Vertenstein, Negin Sobhani, Samuel Levis, David Lawrence, Michael Barlage,

501   Joe Hammann, and Erik Kluzek.

502

503   **Financial support:** This study is supported by COMPASS-GLM, a multi-institutional project supported

504   by the U.S. Department of Energy (DOE), Office of Science, Office of Biological and Environmental

505   Research, Earth and Environmental Systems Modeling program. T.C.'s contribution was also supported by

506   the DOE, Office of Science, Biological and Environmental Research program through an Early Career

507   award. The Pacific Northwest National Laboratory is operated for DOE by Battelle Memorial Institute

508   under contract DE-AC05-76RL01830.

509

510

511

Reference:

Ban-Weiss, G. A., Bala, G., Cao, L., Pongratz, J., and Caldeira, K.: Climate forcing and response to idealized changes in surface latent and sensible heat, Environ Res Lett, 6, 034032, 2011.

Best, M. J., Abramowitz, G., Johnson, H. R., Pitman, A. J., Balsamo, G., Boone, A., Cuntz, M., Decharme, B., Dirmeyer, P. A., Dong, J., Ek, M., Guo, Z., Haverd, V., van den Hurk, B. J. J., Nearing, G. S., Pak, B., Peters-Lidard, C., Santanello, J. A., Stevens, L., and Vuichard, N.: The Plumbing of Land Surface Models: Benchmarking Model Performance, J Hydrometeorol, 16, 1425-1442, https://doi.org/10.1175/JHM-D-14-0158.1, 2015.

Binsted, M., Iyer, G., Patel, P., Graham, N. T., Ou, Y., Khan, Z., Kholod, N., Narayan, K., Hejazi, M., Kim, S., Calvin, K., and Wise, M.: GCAM-USA v5.3_water_dispatch: integrated modeling of subnational US energy, water, and land systems within a global framework, Geosci. Model Dev., 15, 2533-2559, 10.5194/gmd-15-2533-2022, 2022.

Bisht, G., Huang, M., Zhou, T., Chen, X., Dai, H., Hammond, G. E., Riley, W. J., Downs, J. L., Liu, Y., and Zachara, J. M.: Coupling a three-dimensional subsurface flow and transport model with a land surface model to simulate stream–aquifer–land interactions (CP v1.0), Geosci. Model Dev., 10, 4539-4562, 10.5194/gmd-10-4539-2017, 2017.

Burrows, S., Maltrud, M., Yang, X., Zhu, Q., Jeffery, N., Shi, X., Ricciuto, D., Wang, S., Bisht, G., and Tang, J.: The DOE E3SM v1. 1 biogeochemistry configuration: Description and simulated ecosystem-climate responses to historical changes in forcing, J Adv Model Earth Sy, 12, e2019MS001766, 2020.

Calvin, K., Patel, P., Clarke, L., Asrar, G., Bond-Lamberty, B., Cui, R. Y., Di Vittorio, A., Dorheim, K., Edmonds, J., and Hartin, C.: GCAM v5. 1: representing the linkages between energy, water, land, climate, and economic systems, Geosci Model Dev, 12, 677-698, 2019.

Chakraborty, T., Lee, X., and Lawrence, D. M.: Diffuse Radiation Forcing Constraints on Gross Primary Productivity and Global Terrestrial Evapotranspiration, Earth's Future, 10, e2022EF002805, https://doi.org/10.1029/2022EF002805, 2022a.

Chakraborty, T., Venter, Z., Qian, Y., and Lee, X.: Lower urban humidity moderates outdoor heat stress, Agu Advances, 3, e2022AV000729, 2022b.

Chakraborty, T. C., Lee, X., Ermida, S., and Zhan, W.: On the land emissivity assumption and Landsat-derived surface urban heat islands: A global analysis, Remote Sens Environ, 265, 112682, https://doi.org/10.1016/j.rse.2021.112682, 2021.

Chen, J., Qian, Y., Chakraborty, T., and Yang, Z.: Complexities of urban impacts on long-term seasonal trends in a mid-sized arid city, Environmental Research Communications, 2024.

Craig, A. P., Vertenstein, M., and Jacob, R.: A new flexible coupler for earth system modeling developed for CCSM4 and CESM1, The International Journal of High Performance Computing Applications, 26, 31-42, 2012.

Dai, Y., Zeng, X., Dickinson, R. E., Baker, I., Bonan, G. B., Bosilovich, M. G., Denning, A. S., Dirmeyer, P. A., Houser, P. R., Niu, G., Oleson, K. W., Schlosser, C. A., and Yang, Z.-L.: The Common Land Model, B Am Meteorol Soc, 84, 1013-1024, https://doi.org/10.1175/BAMS-84-8-1013, 2003.

Dickinson, R. E.: Modeling evapotranspiration for three-dimensional global climate models, Climate processes and climate sensitivity, 29, 58-72, 1984.

Fang, Y., Leung, L. R., Knox, R., Koven, C., and Bond-Lamberty, B.: Impact of the numerical solution approach of a plant hydrodynamic model (v0.1) on vegetation dynamics, Geosci. Model Dev., 15, 6385-6398, 10.5194/gmd-15-6385-2022, 2022.

Fisher, R. A. and Koven, C. D.: Perspectives on the Future of Land Surface Models and the Challenges of Representing Complex Terrestrial Systems, J Adv Model Earth Sy, 12, e2018MS001453, https://doi.org/10.1029/2018MS001453, 2020.

Fisher, R. A., Muszala, S., Verteinstein, M., Lawrence, P., Xu, C., McDowell, N. G., Knox, R. G., Koven, C., Holm, J., and Rogers, B. M.: Taking off the training wheels: the properties of a dynamic vegetation model without climate envelopes, CLM4. 5 (ED), Geosci Model Dev, 8, 3593-3619, 2015.

Gropp, W., Lusk, E., Doss, N., and Skjellum, A.: A high-performance, portable implementation of the MPI message passing interface standard, Parallel Computing, 22, 789-828, https://doi.org/10.1016/0167-8191(96)00024-5, 1996.

Hao, D., Bisht, G., Gu, Y., Lee, W. L., Liou, K. N., and Leung, L. R.: A parameterization of sub-grid topographical effects on solar radiation in the E3SM Land Model (version 1.0): implementation and evaluation over the Tibetan Plateau, Geosci. Model Dev., 14, 6273-6289, 10.5194/gmd-14-6273-2021, 2021.

Hersbach, H., Bell, B., Berrisford, P., Hirahara, S., Horanyi, A., Munoz-Sabater, J., Nicolas, J., Peubey, C., Radu, R., Schepers, D., Simmons, A., Soci, C., Abdalla, S., Abellan, X., Balsamo, G., Bechtold, P., Biavati, G., Bidlot, J., Bonavita, M., De Chiara, G., Dahlgren, P., Dee, D., Diamantakis, M., Dragani, R., Flemming, J., Forbes, R., Fuentes, M., Geer, A., Haimberger, L., Healy, S., Hogan, R. J., Holm, E., Janiskova, M., Keeley, S., Laloyaux, P., Lopez, P., Lupu, C., Radnoti, G., de Rosnay, P., Rozum, I., Vamborg, F., Villaume, S., and Thepaut, J. N.: The ERA5 global reanalysis, Q J Roy Meteor Soc, 146, 1999-2049, 10.1002/qj.3803, 2020.

Hill, C., DeLuca, C., Suarez, M., and Da Silva, A.: The architecture of the earth system modeling framework, Computing in Science & Engineering, 6, 18-28, 2004.

Hong, S.-Y. and Lim, J.-O. J.: The WRF single-moment 6-class microphysics scheme (WSM6), Asia-Pacific Journal of Atmospheric Sciences, 42, 129-151, 2006.

Huang. H.: ELM code within WRF-ELM. Zenodo. https://doi.org/10.5281/zenodo.11289807, 2024

Huang, H., Xue, Y., Li, F., and Liu, Y.: Modeling long-term fire impact on ecosystem characteristics and surface energy using a process-based vegetation–fire model SSiB4/TRIFFID-Fire v1.0, Geosci Model Dev, 13, 6029-6050, 10.5194/gmd-13-6029-2020, 2020a.

Huang, H., Xue, Y., Liu, Y., Li, F., and Okin, G. S.: Modeling the short-term fire effects on vegetation dynamics and surface energy in southern Africa using the improved SSiB4/TRIFFID-Fire model, Geosci Model Dev, 14, 7639-7657, 10.5194/gmd-14-7639-2021, 2021.

Huang, H., Xue, Y., Chilukoti, N., Liu, Y., Chen, G., and Diallo, I.: Assessing Global and Regional Effects of Reconstructed Land-Use and Land-Cover Change on Climate since 1950 Using a Coupled Land–Atmosphere–Ocean Model, J Climate, 33, 8997-9013, 10.1175/jcli-d-20-0108.1, 2020b.

Iacono, M. J., Delamere, J. S., Mlawer, E. J., Shephard, M. W., Clough, S. A., and Collins, W. D.: Radiative forcing by long-lived greenhouse gases: Calculations with the AER radiative transfer models, Journal of Geophysical Research: Atmospheres, 113, https://doi.org/10.1029/2008JD009944, 2008.

Jacob, R., Larson, J., and Ong, E.: M× N communication and parallel interpolation in Community Climate System Model Version 3 using the model coupling toolkit, The International Journal of High Performance Computing Applications, 19, 293-307, 2005.

Jenkinson, D. S.: The turnover of organic carbon and nitrogen in soil, Philosophical Transactions of the Royal Society of London. Series B: Biological Sciences, 329, 361-368, 1990.

Kayastha, M. B., Huang, C., Wang, J., Pringle, W. J., Chakraborty, T. C., Yang, Z., Hetland, R. D., Qian, Y., and Xue, P.: Insights on Simulating Summer Warming of the Great Lakes: Understanding the Behavior of a Newly Developed Coupled Lake-Atmosphere Modeling System, J Adv Model Earth Sy, 15, e2023MS003620, https://doi.org/10.1029/2023MS003620, 2023.

Krayenhoff, E. S., Jiang, T., Christen, A., Martilli, A., Oke, T. R., Bailey, B. N., Nazarian, N., Voogt, J. A., Giometto, M. G., and Stastny, A.: A multi-layer urban canopy meteorological model with trees (BEP-Tree): Street tree impacts on pedestrian-level climate, Urban Climate, 32, 100590, 2020.

Larson, J., Jacob, R., and Ong, E.: The model coupling toolkit: A new Fortran90 toolkit for building multiphysics parallel coupled models, The International Journal of High Performance Computing Applications, 19, 277-292, 2005.

Law, B.: Carbon dynamics in response to climate and disturbance: Recent progress from multi-scale measurements and modeling in AmeriFlux, Plant responses to air pollution and global change, 205-213, 2005.

Lawrence, D. M., Fisher, R. A., Koven, C. D., Oleson, K. W., Swenson, S. C., Bonan, G., Collier, N., Ghimire, B., van Kampenhout, L., Kennedy, D., Kluzek, E., Lawrence, P. J., Li, F., Li, H., Lombardozzi,

D., Riley, W. J., Sacks, W. J., Shi, M., Vertenstein, M., Wieder, W. R., Xu, C., Ali, A. A., Badger, A. M., Bisht, G., van den Broeke, M., Brunke, M. A., Burns, S. P., Buzan, J., Clark, M., Craig, A., Dahlin, K., Drewniak, B., Fisher, J. B., Flanner, M., Fox, A. M., Gentine, P., Hoffman, F., Keppel-Aleks, G., Knox, R., Kumar, S., Lenaerts, J., Leung, L. R., Lipscomb, W. H., Lu, Y., Pandey, A., Pelletier, J. D., Perket, J., Randerson, J. T., Ricciuto, D. M., Sanderson, B. M., Slater, A., Subin, Z. M., Tang, J., Thomas, R. Q., Val Martin, M., and Zeng, X.: The Community Land Model Version 5: Description of New Features, Benchmarking, and Impact of Forcing Uncertainty, J Adv Model Earth Sy, 11, 4245-4287, https://doi.org/10.1029/2018MS001583, 2019.

Li, C., Frolking, S., and Frolking, T. A.: A model of nitrous oxide evolution from soil driven by rainfall events: 1. Model structure and sensitivity, Journal of Geophysical Research: Atmospheres, 97, 9759-9776, 1992.

Li, F., Zeng, X. D., and Levis, S.: A process-based fire parameterization of intermediate complexity in a Dynamic Global Vegetation Model, Biogeosciences, 9, 2761-2780, 10.5194/bg-9-2761-2012, 2012.

Li, L., Bisht, G., Hao, D., and Leung, L. R.: Global 1 km land surface parameters for kilometer-scale Earth system modeling, Earth Syst. Sci. Data, 16, 2007-2032, 10.5194/essd-16-2007-2024, 2024.

Lin, Y. and Mitchell, K. E.: 1.2 the NCEP stage II/IV hourly precipitation analyses: Development and applications, Proceedings of the 19th Conference Hydrology, American Meteorological Society, San Diego, CA, USA,

Liu, Y., Xue, Y., MacDonald, G., Cox, P., and Zhang, Z.: Global vegetation variability and its response to elevated CO_2, global warming, and climate variability – a study using the offline SSiB4/TRIFFID model and satellite data, Earth Syst. Dynam., 10, 9-29, 10.5194/esd-10-9-2019, 2019.

Martín Belda, D., Anthoni, P., Wårlind, D., Olin, S., Schurgers, G., Tang, J., Smith, B., and Arneth, A.: LPJ-GUESS/LSMv1.0: a next-generation land surface model with high ecological realism, Geosci. Model Dev., 15, 6709-6745, 10.5194/gmd-15-6709-2022, 2022.

Muñoz-Sabater, J.: ERA5-Land monthly averaged data from 1950 to present., Copernicus Climate Change Service (C3S) Climate Data Store (CDS). [dataset], 10.24381/cds.68d2bb30, 2019.

Muñoz-Sabater, J., Dutra, E., Agustí-Panareda, A., Albergel, C., Arduini, G., Balsamo, G., Boussetta, S., Choulga, M., Harrigan, S., Hersbach, H., Martens, B., Miralles, D. G., Piles, M., Rodríguez-Fernández, N. J., Zsoter, E., Buontempo, C., and Thépaut, J. N.: ERA5-Land: a state-of-the-art global reanalysis dataset for land applications, Earth Syst. Sci. Data, 13, 4349-4383, 10.5194/essd-13-4349-2021, 2021.

Nadolski, V.: Automated surface observing system user's guide, NOAA Publ, 12, 94, 1992.

Nelson, B. R., Prat, O. P., Seo, D. J., and Habib, E.: Assessment and Implications of NCEP Stage IV Quantitative Precipitation Estimates for Product Intercomparisons, Weather and Forecasting, 31, 371-394, https://doi.org/10.1175/WAF-D-14-00112.1, 2016.

Oleson, K. and Feddema, J.: Parameterization and surface data improvements and new capabilities for the Community Land Model Urban (CLMU), J Adv Model Earth Sy, 12, e2018MS001586, 2020.

Parton, W. J., Stewart, J. W., and Cole, C. V.: Dynamics of C, N, P and S in grassland soils: a model, Biogeochemistry, 5, 109-131, 1988.

Paschalis, A., Chakraborty, T., Fatichi, S., Meili, N., and Manoli, G.: Urban forests as main regulator of the evaporative cooling effect in cities, AGU Advances, 2, e2020AV000303, 2021.

Pelosi, A., Terribile, F., D'Urso, G., and Chirico, G. B.: Comparison of ERA5-Land and UERRA MESCAN-SURFEX reanalysis data with spatially interpolated weather observations for the regional assessment of reference evapotranspiration, Water, 12, 1669, 2020.

Qiu, H., Bisht, G., Li, L., Hao, D., and Xu, D.: Development of inter-grid-cell lateral unsaturated and saturated flow model in the E3SM Land Model (v2.0), Geosci. Model Dev., 17, 143-167, 10.5194/gmd-17-143-2024, 2024.

Rizwan, A. M., Dennis, L. Y., and Chunho, L.: A review on the generation, determination and mitigation of Urban Heat Island, Journal of environmental sciences, 20, 120-128, 2008.

Schwab, D. J., Leshkevich, G. A., and Muhr, G. C.: Satellite Measurements of Surface Water Temperature in the Great Lakes: Great Lakes Coastwatch, Journal of Great Lakes Research, 18, 247-258, https://doi.org/10.1016/S0380-1330(92)71292-1, 1992.

Sellers, P., Mintz, Y., Sud, Y. e. a., and Dalcher, A.: A simple biosphere model (SiB) for use within general circulation models, J Atmos Sci, 43, 505-531, 1986.

Sinha, E., Bond-Lamberty, B., Calvin, K. V., Drewniak, B. A., Bisht, G., Bernacchi, C., Blakely, B. J., and Moore, C. E.: The Impact of Crop Rotation and Spatially Varying Crop Parameters in the E3SM Land Model (ELMv2), Journal of Geophysical Research: Biogeosciences, 128, e2022JG007187, https://doi.org/10.1029/2022JG007187, 2023.

Skamarock, W. C. and Klemp, J. B.: A time-split nonhydrostatic atmospheric model for weather research and forecasting applications, Journal of Computational Physics, 227, 3465-3485, https://doi.org/10.1016/j.jcp.2007.01.037, 2008.

Soltani, A. and Sharifi, E.: Daily variation of urban heat island effect and its correlations to urban greenery: A case study of Adelaide, Frontiers of Architectural Research, 6, 529-538, https://doi.org/10.1016/j.foar.2017.08.001, 2017.

Stefanidis, K., Varlas, G., Vourka, A., Papadopoulos, A., and Dimitriou, E.: Delineating the relative contribution of climate related variables to chlorophyll-a and phytoplankton biomass in lakes using the ERA5-Land climate reanalysis data, Water research, 196, 117053, 2021.

Team, C. D.: ESCOMP/CTSM: release-clm5.0.37 (release-clm5.0.37) [dataset], https://doi.org/10.5281/zenodo.11176755, 2024.

Thompson, G., Rasmussen, R. M., and Manning, K.: Explicit Forecasts of Winter Precipitation Using an Improved Bulk Microphysics Scheme. Part I: Description and Sensitivity Analysis, Mon Weather Rev, 132, 519-542, https://doi.org/10.1175/1520-0493(2004)132<0519:EFOWPU>2.0.CO;2, 2004.

Thompson, G., Field, P. R., Rasmussen, R. M., and Hall, W. D.: Explicit Forecasts of Winter Precipitation Using an Improved Bulk Microphysics Scheme. Part II: Implementation of a New Snow Parameterization, Mon Weather Rev, 136, 5095-5115, https://doi.org/10.1175/2008MWR2387.1, 2008.

Thonicke, K., Spessa, A., Prentice, I. C., Harrison, S. P., Dong, L., and Carmona-Moreno, C.: The influence of vegetation, fire spread and fire behaviour on biomass burning and trace gas emissions: results from a process-based model (vol 7, pg 1991, 2010), Biogeosciences, 7, 2191-2191, 10.5194/bg-7-2191-2010, 2010.

Thornton, M., Shrestha, R., Wei, Y., Thornton, P., Kao, S., and Wilson, B.: Daymet: Daily Surface Weather Data on a 1-km Grid for North America, Version 4 R1. ORNL DAAC, Oak Ridge, Tennessee, USA., https://doi.org/10.3334/ORNLDAAC/2129, 2022.

UCAR: Using CTSM with WRF — CTSM documentation., https://escomp.github.io/ctsm-docs/versions/master/html/lilac/specific-atm-models/wrf.html, 2020.

Wang, J., Xue, P., Pringle, W., Yang, Z., and Qian, Y.: Impacts of Lake Surface Temperature on the Summer Climate Over the Great Lakes Region, Journal of Geophysical Research: Atmospheres, 127, e2021JD036231, https://doi.org/10.1029/2021JD036231, 2022a.

Wang, J., Qian, Y., Pringle, W., Chakraborty, T. C., Hetland, R., Yang, Z., and Xue, P.: Contrasting effects of lake breeze and urbanization on heat stress in Chicago metropolitan area, Urban Climate, 48, 101429, https://doi.org/10.1016/j.uclim.2023.101429, 2023.

Wang, Y.-R., Hessen, D. O., Samset, B. H., and Stordal, F.: Evaluating global and regional land warming trends in the past decades with both MODIS and ERA5-Land land surface temperature data, Remote Sens Environ, 280, 113181, https://doi.org/10.1016/j.rse.2022.113181, 2022b.

Weng, E., Malyshev, S., Lichstein, J., Farrior, C. E., Dybzinski, R., Zhang, T., Shevliakova, E., and Pacala, S. W.: Scaling from individual trees to forests in an Earth system modeling framework using a mathematically tractable model of height-structured competition, Biogeosciences, 12, 2655-2694, 2015.

Wiltshire, A. J., Duran Rojas, M. C., Edwards, J. M., Gedney, N., Harper, A. B., Hartley, A. J., Hendry, M. A., Robertson, E., and Smout-Day, K.: JULES-GL7: the Global Land configuration of the Joint UK Land Environment Simulator version 7.0 and 7.2, Geosci. Model Dev., 13, 483-505, 10.5194/gmd-13-483-2020, 2020.

Xia, Y., Mitchell, K., Ek, M., Sheffield, J., Cosgrove, B., Wood, E., Luo, L., Alonge, C., Wei, H., Meng, J., Livneh, B., Lettenmaier, D., Koren, V., Duan, Q., Mo, K., Fan, Y., and Mocko, D.: Continental-scale water and energy flux analysis and validation for the North American Land Data Assimilation System project

713   phase 2 (NLDAS-2): 1. Intercomparison and application of model products, Journal of Geophysical
714   Research: Atmospheres, 117, https://doi.org/10.1029/2011JD016048, 2012.

715   Xu, C., Christoffersen, B., Robbins, Z., Knox, R., Fisher, R. A., Chitra-Tarak, R., Slot, M., Solander, K.,
716   Kueppers, L., Koven, C., and McDowell, N.: Quantification of hydraulic trait control on plant
717   hydrodynamics and risk of hydraulic failure within a demographic structured vegetation model in a tropical
718   forest (FATES–HYDRO V1.0), Geosci. Model Dev., 16, 6267-6283, 10.5194/gmd-16-6267-2023, 2023.

719   Xue, Y., Sellers, P. J., Kinter, J. L., and Shukla, J.: A Simplified Biosphere Model for Global Climate Studies,
720   J Climate, 4, 345-364, https://doi.org/10.1175/1520-0442(1991)004<0345:ASBMFG>2.0.CO;2, 1991.

721   Yuan, F., Wang, D., Kao, S.-C., Thornton, M., Ricciuto, D., Salmon, V., Iversen, C., Schwartz, P., and
722   Thornton, P.: An ultrahigh-resolution E3SM land model simulation framework and its first application to
723   the Seward Peninsula in Alaska, Journal of Computational Science, 73, 102145, 2023.

724